Indian Journal of Chemistry
Vol. 63, August 2024, pp. 782-790
DOI: 10.56042/ijc.v63i8.8566

Flower-like $NiCo_2S_4$/rGO composites directly grown on Ni foam as highly efficient electrode for long cycling stability supercapacitor

Yongfu Zhao*, Shuaijun Han & Hui Liu
College of Chemistry and Chemical Engineering, Zhengzhou Normal University, Zhengzhou 450044, P R China
E-mail: zhaoyongfu2008@163.com

Received 5 February 2024; accepted (revised) 22 May 2024

$NiCo_2S_4$ and reduced graphene oxide(rGO) have been directly grown on Ni foam by a two-step hydrothermal method to form $NiCo_2S_4$/rGO composite material with hierarchical structures. The resulting samples display flower-like $NiCo_2S_4$ particles formed by interconnected $NiCo_2S_4$ nanosheets with the conductive rGO sheets interspersing among them. This unique structure can provide a much rougher surface, rich two-phase interface, and porous channels exposed to electrolytes with fast ion diffusions and electron transmissions, as well as effectively relieve the expansion/contractions during charging and discharging. The electrochemical test results show that $NiCo_2S_4$/rGO composite prepared at 120°C with 8.1 mg mass loading on Ni foam exhibits a specific capacitance (1974.7 $F\cdot g^{-1}$) at a current density of 10 $mA\cdot cm^{-2}$. An asymmetric supercapacitor device assembled by $NiCo_2S_4$/rGO and activated carbon can provide an energy density high up to 46.8 $Wh\cdot kg^{-1}$ at a power density of 219.5 $W\cdot kg^{-1}$. Even if the power density is increased up to 731.6 W kg^{-1}, it still can achieve the energy density superior to 31.8 Wh kg^{-1}. Moreover, the asymmetric supercapacitor device exhibits an outstanding cycling stability with 87.8% capacitance retention after 5000 cycles, which confirms its potential application in the energy storage.

Keywords: Flower-like composite, RGO, $NiCo_2S_4$/rGO composite, Asymmetric supercapacitor

Supercapacitors, also known as electrochemical capacitors (ECs), with high power density, fast charge-discharge and good cycle performance, have attracted immense attention as important energy storage devices for potential applications in hybrid electric vehicles and portable electronic devices[1-3]. In the development of high-performance supercapacitors, electrode materials play an essential role. Therefore, most researchers have focused on developing different active electrode materials for supercapacitors based on transition metal oxides/sulfides (TMOSs), carbon-based materials, and conducting polymers[4-7].

Carbonaceous materials store energy through pure electrostatic charge accumulation at electrode electrolyte interfaces arising from electrical double layer capacitance (EDLC). These materials have high power density, good electrical conductivity and outstanding stability, yet, they suffer from low specific capacitance, which limits their applications for high energy density[8]. In contrast, TMOSs and conductive polymers store energy through rapid and reversible redox or Faradaic charge reactions on the electrode's surface, which can provide higher specific capacitance than that of EDLC. However, the conductive polymers undergo volume shrinkage and expansion upon charging and discharging cycles, resulting in poor cycle stability[9]. Compared to the conductive polymers, TMOSs increasingly become good fundamental candidates for ECs due to high theoretical capacity, wide voltage range and good electrochemical stability[10-14]. Among the various TMOSs, Spinel nickel cobaltite ($NiCo_2O_4$) has attracted great attention due to the ultrahigh energy storage capacity, outstanding cycling stability and low resistance[15,16]. Compared to monometallic compounds such as NiO and Co_3O_4, the bimetallic spinel compounds exhibit more oxidation states that enable multiple redox reactions from both nickel and cobalt ions. In addition to metal oxides, metal sulfides are also drawing increasing attention. Replacing the oxygen with sulfur that has a lower electronegativity and more flexible structure enables a more facile transport of electrons, leading to enhanced power performance of the devices[17]. For example, compared to $NiCo_2O_4$, $NiCo_2S_4$ has been reported to possess much higher conductivity[18]. Although $NiCo_2S_4$ exhibits better conductivity compared to the corresponding oxides, it is still lower for $NiCo_2S_4$ to achieve its theoretical capacity in practical applications. Therefore, an effective approach to enhance its experimental capacitance is by hybridizing $NiCo_2S_4$ with conductive materials, especially, carbonaceous materials[19,20].

Due to its superior surface area, superb mechanical properties, and outstanding electronic conductivity, rGO is considered promising candidates to enhance the electronic conductivity of composites. Moreover, providing a layer of rGO nanosheets can add active sites to achieve maximized utilization of pseudocapacitive $NiCo_2S_4$. The excellent adhesion between $NiCo_2S_4$ and rGO helps control the distribution of $NiCo_2S_4$ on the rGO surface, preventing aggregation and providing short diffusion channels for both ions and electrons, which led to high electronic conductivity for the nanocomposite[21]. For example, Nguyen[22] prepared 3D rGO/$NiCo_2S_4$ aerogels by a one-step hydrothermal approach, achieving a maximum specific capacitance of 813 $F\cdot g^{-1}$ at 1.5 $A\cdot g^{-1}$. Li[23] demonstrated that $NiCo_2S_4$ nanoparticles anchored on reduced graphene oxide sheets show a high specific capacitance of 1804.7 $F\cdot g^{-1}$ at a current density of 0.5 $A\cdot g^{-1}$. The improved electrochemical performances are attributed to the increased conductivity in the presence of rGO and the enhanced effective interfacial area caused by $NiCo_2S_4$ nanoparticles homogeneously grown on the surface of rGO sheets. It is also demonstrated that $NiCo_2S_4$ in-situ grown on suitable substrates (Ni foam or carbon cloth) can increase the active surface area, shorten the charge transfer path, and avoid using any binders, which are beneficial to improve the electrochemical performance[24-26].

In this work, the flower-like $NiCo_2S_4$ particles anchored on rGO sheets were directly grown on Ni foam by a two-step hydrothermal method by adjusting conditions of hydrothermal process. The introduction of rGO provided an abundance of active locations for the growth of metal ions due to its greater specific surface area. As a result, $NiCo_2S_4$ particles formed by interconnected $NiCo_2S_4$ nanosheets were uniformly grown on rGO sheets, and the excellent adhesion between $NiCo_2S_4$ and rGO helps prevent aggregation with each other. The $NiCo_2S_4$/rGO revealed excellent electrochemical performance with a specific capacitance of 1974.7 $F\cdot g^{-1}$ at a current density of 10 $mA\cdot cm^{-2}$. The $NiCo_2S_4$/rGO-based supercapacitors exhibit high energy/power density and an outstanding cycling stability. The above excellent electrochemical performance of $NiCo_2S_4$/rGO composites is suggested to be attributed to their unique particle-sheet structure with an enlarged surface area, flexible conductive rGO network for effective charge access and propagation.

Experimental Section

Reagents and Materials

Ni foam was acquired from Shenzhen Teensky Technology Co., Ltd. rGO (<6 layers) obtained from Chengdu Organic Chemicals Co. Ltd., Chinese Academy of Sciences. $Ni(NO_3)_2\cdot 6H_2O$, $Co(NO_3)_2\cdot 6H_2O$, ammonium fluoride and thioacetamide were purchased from Tianjin Kemiou Chemical Reagent Co., Ltd. All reagents were of analytical grade and used without further purification.

Synthesis of $NiCo_2S_4$/ rGO on Ni foam

First of all, Ni foam (2×1 cm) was pretreated with acetone, hydrochloric acid and deionized (DI) water successively to remove surface impurities and oxides, then dried in the electrical oven. The $NiCo_2S_4$/rGO composites were prepared using a facile two-step hydrothermal method. For the first hydrothermal step, 0.75 g of polyvinyl pyrrolidinone and 30 mg of rGO were dissolved in 70 mL DI water under ultrasonic condition. Then, 2 mmol $Ni(NO_3)_2\cdot 6H_2O$, 4 mmol $Co(NO_3)_2\cdot 6H_2O$, 12mmol NH_4F and 24 mmol urea were added into above mixture and stirred vigorously for 1 h. Subsequently, the resulting mixture was transferred into a 100 ml Teflon-lined stainless-steel autoclave. Three pieces of nickel foams were immersed in the solution followed by heating of the autoclave at 120°C for 10 h. After cooling down to room temperature, the Ni-Co precursor on Ni foam was washed with ethanol and DI water, then dried at 60°C for 6h. For the second hydrothermal step, firstly, 25 mmol of urea and 5 mmol of thioacetamide were added into 70 mL of DI water and stirred for 30 min to obtain a homogenous solution. Then, above solution and the Ni-Co precursor on Ni foam were transferred into a 100 ml Teflon-lined stainless-steel autoclave and heated at 140°C for 8 h. Finally, the $NiCo_2S_4$/rGO composites on Ni foam were washed by ethanol and DI water, and then dried at 60°C for 12 h. For comparison, the Ni foams loaded with only $NiCo_2S_4$ were prepared by the same procedure in absence of rGO in the first hydrothermal step.

Assembly of asymmetric supercapacitors

Activated carbon (AC) was mixed with acetylene black and poly vinylidene fluoride at a 70:20:10 wt ratio in N-methyl-2-pyrrolidone to form an active-material paste. The active-material paste was coated on a Ni foam and dried at 60°C for 12 h, forming a negative electrode. An asymmetric supercapacitor (ASC) was assembled using the Ni foam loaded with $NiCo_2S_4$/rGO composite as positive electrode, AC electrode as a negative electrode, and 6 M KOH solution as an electrolyte.

Materials characterization

The morphology were investigated by using field emission scanning electron microscope (FESEM, Hitachi S-4800). X-ray diffraction (XRD) measurements were performed on a Rigaku D/MAX-2400 X-ray diffractometer using Cu Kα radiation. FT-IR spectrum of the $NiCo_2S_4$/rGO composites was recorded with a Nicolet 380 FT-IR spectrophotometer.

Electrochemical characterization

Electrochemical measurement of $NiCo_2S_4$ and $NiCo_2S_4$/rGO electrodes was performed in a three-electrode system with a silver/silver chloride (Ag/AgCl) reference electrode and a platinum (Pt) counter electrode in 6 M KOH as the aqueous electrolyte, in an electrochemical workstation (CHI660E). Experiments were implemented to determine the cyclic voltammetry (CV) curves, the galvanostatic charge/discharge (GCD) curves, the cycle life, and the electrochemical impedance spectroscopy (EIS). The electrochemical supercapacitor performance of the $NiCo_2S_4$/rGO composite was determined in an asymmetric supercapacitor. The specific capacitance of the devices was calculated according to the equation 1:

$$C = \frac{i \times \Delta t}{m \times \Delta V} \qquad \ldots(1)$$

where, C (F g^{-1}) stands for specific capacitance, i is the discharge current, Δt is the discharge period of time, m is the mass of the active material in the electrode, and ΔV is the operational voltage window of the electrode.

The active substances of positive and negative electrode materials shall meet the charge balance equation (2):

$$\frac{m_+}{m_-} = \frac{C_+ \times \Delta V_+}{C_- \times \Delta V_-} \qquad \ldots(2)$$

where, “+” and “–” represent the positive and negative electrodes, respectively.

The energy and power density values were subsequently calculated by equation 3 and equation 4, respectively.

$$E = \frac{C \times \Delta V^2}{2 \times 3.6} \qquad \ldots(3)$$

$$P = \frac{3600E}{\Delta t} \qquad \ldots(4)$$

where, E (Wh·kg^{-1}) is the energy density, C is the specific capacitance of the asymmetric supercapacitor, P (W·kg^{-1}) is the power density[16,27].

Results and Discussion

XRD patterns analysis

The phase composition of the samples is analyzed by XRD. Fig. 1a illustrates the XRD patterns of the rGO, $NiCo_2S_4$ and $NiCo_2S_4$/rGO composite. It can be seen that rGO has characteristic peak in the range of 20°-30°,

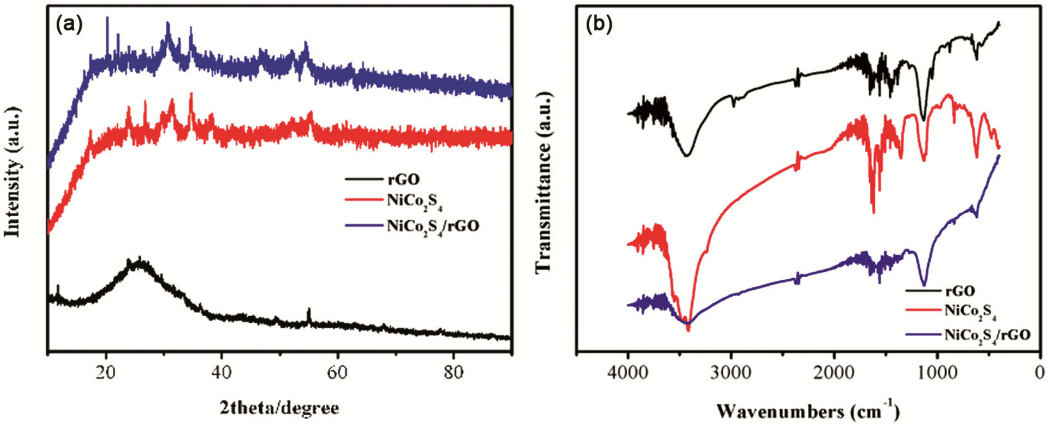

Fig. 1 — (a) XRD patterns of graphene, $NiCo_2S_4$ and $NiCo_2S_4$/rGO composite. (b) FT-IR spectra of graphene, $NiCo_2S_4$ and $NiCo_2S_4$/rGO composite.

corresponding to the (002) crystal plane. The pattern profiles indicate four diffraction peaks at 2θ value of 26.8°, 31.6°, 38.3° and 55.3°, which correspond to (220), (311), (400) and (440) planes of the $NiCo_2S_4$ cubic crystal phase, respectively[28]. In addition to the peaks at 26.8°, 31.6°, 38.3° and 55.3°, The XRD pattern of the $NiCo_2S_4$/rGO composite displays an obscure peak in the range of 20° to 30°, indicating that rGO has compounded with $NiCo_2S_4$ effectively.

FT-IR spectroscopic analysis

FT-IR spectra of rGO, $NiCo_2S_4$ and $NiCo_2S_4$/rGO composite are shown in Fig. 1b. In the FT-IR spectrum of rGO, peaks at 3400 cm^{-1},1625 cm^{-1} and 1065 cm^{-1} are attributed to the stretching vibration of -OH, -C=C, and the asymmetric stretching vibration of C-O-C, respectively. From the spectrum of $NiCo_2S_4$, the peak at 3400 cm^{-1} may be due to the stretching vibration of -OH of the precursor or H_2O. From the FT-IR spectra of $NiCo_2S_4$ and $NiCo_2S_4$/rGO the peaks at 613, 585 cm^{-1}(symmetrical stretch) and 1084 cm^{-1} (asymmetrical stretch) are generated by the vibration of Co-S or Ni-S of $NiCo_2S_4$ [29]. The characteristic peaks of rGO, Ni-S and Co-S can be found in the spectrum of the $NiCo_2S_4$/rGO composite, with the peak asymmetric stretching vibration of C-O-C overlapping the peak of Co-S at near 1070 cm^{-1}. The FT-IR analysis of the composite is consistent with the XRD result that rGO has compound with $NiCo_2S_4$ effectively.

$NiCo_2S_4$/rGO composite characterization with SEM

The morphology of the $NiCo_2S_4$ and $NiCo_2S_4$/rGO grown on Ni foam were investigated by scanning electron microscopy (SEM), the results are presented in Fig. 2. Fig. 2(a, b) clearly illustrates the compact structure of $NiCo_2S_4$ and loose $NiCo_2S_4$/rGO composite nanoparticles are grown on Ni-foam by hydrothermal method, respectively. As shown in Fig. 2 (c, d), the pristine $NiCo_2S_4$ exhibits nanoplate structure packed on the Ni foam. In comparison with pristine $NiCo_2S_4$, $NiCo_2S_4$/rGO displays a more obvious loose particle structure with rGO sheets interspersing among $NiCo_2S_4$ particles. Fig. 2(e, f) presents more detailed inner structure for pristine $NiCo_2S_4$ and $NiCo_2S_4$/rGO composite. The $NiCo_2S_4$ nanoplate in pristine $NiCo_2S_4$ closely arranges to form a brick wall-like structure, whereas $NiCo_2S_4$ in $NiCo_2S_4$/rGO composite displays flower-like particle formed by $NiCo_2S_4$ nanosheets interconnected with each other. As shown in Fig. 2f, the interconnected $NiCo_2S_4$ nanosheets have a thickness of approximately 25 nm, which is favorable for full utilization of the active materials. The reason that the morphology of $NiCo_2S_4$/rGO composite differs from pristine $NiCo_2S_4$ is that rGO can offer substantial active sites for nucleation of $NiCo_2S_4$ nanoparticles and confines growth of $NiCo_2S_4$ by taking the advantages of high specific surface area and porosity of rGO[30].

Electrochemical performances of $NiCo_2S_4$/rGO composite

Fig. 3a exhibits CV curves of Ni foam, $NiCo_2S_4$ and $NiCo_2S_4$/rGO composite electrodes at 5 $mV\cdot s^{-1}$. As can be seen from the figure, the CV curve of the Ni foam shows no distinct redox peak and possesses smaller enclosed area, indicating that the contribution

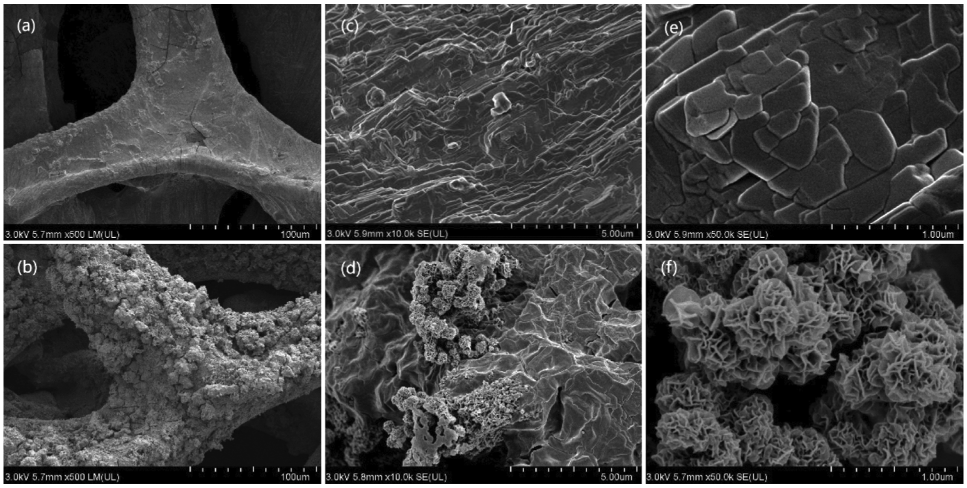

Fig. 2 — SEM images at different magnifications of (a, c and e) $NiCo_2S_4$ supported on Ni foam and (b, d and f) $NiCo_2S_4$/rGO grown on Ni foam, respectively.

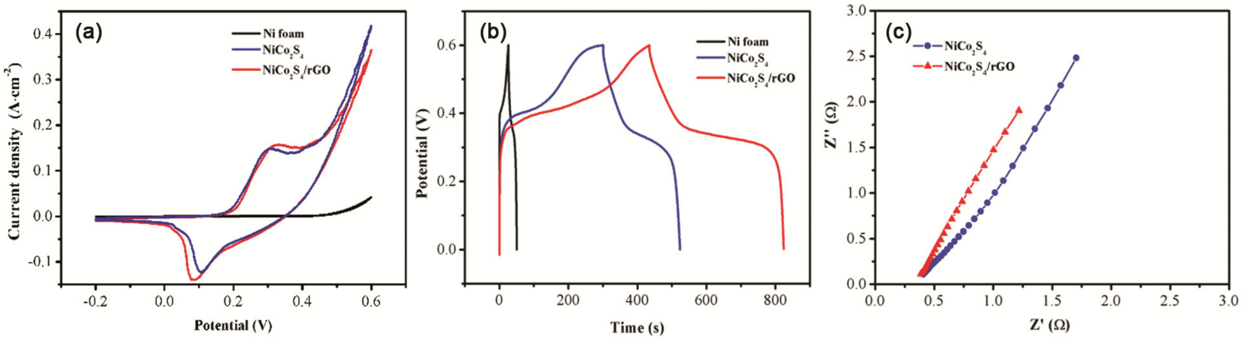

Fig. 3 — CV curves at 5 mV·s^{-1} (a) and GCD curves at 10 mA·cm^{-2} (b) for three electrodes. (c) Nyquist impedance spectra of $NiCo_2S_4$ and $NiCo_2S_4$/rGO composite electrodes.

of Ni foam on the specific capacity of $NiCo_2S_4$/rGO composite is negligible. Both $NiCo_2S_4$ and $NiCo_2S_4$/rGO composite electrodes exhibit a pair of distinct redox peaks, which is indicative of a typical pseudocapacitive behavior of $NiCo_2S_4$. Moreover, the $NiCo_2S_4$/rGO composite electrode has a larger integrated area of CV curves than that of $NiCo_2S_4$ at the same scan rates, suggesting that it has a better charge storage capacity.

GCD tests of Ni foam, $NiCo_2S_4$ and $NiCo_2S_4$/rGO composite electrodes were performed at a current density of 10 mA·cm^{-2}, and results were shown in Fig. 3b. The symmetric shape of the GCD curves of $NiCo_2S_4$ and $NiCo_2S_4$/rGO composite electrodes with a potential window of 0-0.6 V implies good electrochemical capacitive characteristics and excellent reversibility of Faradaic redox reactions. The obvious charging/discharging plateaus can verify their battery charge storage behaviour, which can be ascribed to the redox reaction of $NiCo_2S_4$ with OH^-. At the same current density, the $NiCo_2S_4$/rGO composite electrode has the longer discharge time, indicating that it possesses a greatly higher specific capacitance than that of $NiCo_2S_4$. This improvement in capacitance is due to the superior electrical conductivity of the rGO, which operates as a highly conductive network for electron transport on the electrode surface during Faradaic reactions[31]. In addition, the excellent adhesion between $NiCo_2S_4$ and rGO helps control the distribution of $NiCo_2S_4$ on the rGO surface, prohibiting aggregation of $NiCo_2S_4$ particles and provides more active sites[21]. Therefore, the $NiCo_2S_4$/rGO composite electrode has excellent capacitance performance.

Fig. 3c shows the Nyquist curves of $NiCo_2S_4$ and $NiCo_2S_4$/rGO composite electrodes measured by electrochemical impedance spectroscopy (EIS). The intercept on real axis in the high frequency region represents the internal resistance (Rs) of the material itself, diameter of semicircle in the middle frequency region represents the contribution of the charge transfer resistance and EDLC. The $NiCo_2S_4$/rGO electrode exhibits lower Rs (0.33 Ω) than the $NiCo_2S_4$ electrode (0.46 Ω), indicating higher conductivity. In the middle frequency region, the $NiCo_2S_4$/rGO composite electrode has no obvious semicircle, suggesting that the $NiCo_2S_4$/rGO composite electrode has faster electron transfer and the EDLC provided by rGO in the electrochemical reaction process[32,33]. The $NiCo_2S_4$/rGO composite electrode exhibits lower charge transfer resistance and internal resistance in that the synergistic effect between rGO and $NiCo_2S_4$ improves the transfer of OH^- from electrolyte to $NiCo_2S_4$ particles and the rapid transfer of charge from $NiCo_2S_4$ particles to Ni foam[34].

Effect of the loading on the electrochemical properties

In order to further understand effect of the $NiCo_2S_4$/rGO loading on the electrochemical performance of the $NiCo_2S_4$/rGO composite electrode, the $NiCo_2S_4$/rGO composite electrodes with different mass loadings (1.9, 3.6, 4.4, 8.1 and 11.5 mg) were prepared by adjusting the concentration of $Co(NO_3)_2$ and $Ni(NO_3)_2$·in hydrothermal reaction. The GCD curves of different loadings at a current density of 10 mA·cm^{-2} are shown in Fig. 4a. A gradual change of capacitive behavior is observed from typical GCD curves related to EDLC behavior at low loadings (1.9 and 3.2 mg) to the $NiCo_2S_4$ pseudocapacitive characteristics at high loadings (8.1 and 11.5 mg). Moreover, the plateau regions in the GCD curves extend with the increase of $NiCo_2S_4$ content, which indicates an increment in capacitance. The specific capacitance of the $NiCo_2S_4$/rGO composite electrodes with different loadings can be calculated from the

GCD curves, and the graph of specific capacitance *vs* loading of $NiCo_2S_4$ is shown in Fig. 4b. At low concentration of $Co(NO_3)_2$ and $Ni(NO_3)_2$, the less nuclei might directly grow into large $NiCo_2S_4$ particles over rGO, which is responsible for the decline of specific capacitance. The specific capacitance of the $NiCo_2S_4$/rGO composite electrode with average loading 8.1 mg reaches a maximum of 1708.3 $F{\cdot}g^{-1}$, whereas, that of the loading 11.5 mg is only 1179.7 $F{\cdot}g^{-1}$. The reason for decrease in capacitance may be due to incomplete reaction of $NiCo_2S_4$ during the electrochemical redox process that starts from the surface of $NiCo_2S_4$ particles, especially for agglomerated large particles[35].

Effect of the hydrothermal temperature on the electrochemical properties

The hydrothermal temperature can regulate the specific surface area, micromorphology and mesoporous volume of the composite, all of which have strong effect on the specific capacitance[36]. Therefore, the GCD test of the $NiCo_2S_4$/rGO composite electrodes prepared at different hydrothermal temperature of the first step was carried out. As shown in Fig. 5a, all GCD curves display two defined voltage plateaus, further indicating that the battery-type faradaic process is responsible for the energy storage. Based on the GCD test the specific capacitance values of the $NiCo_2S_4$/rGO composite electrodes prepared at different hydrothermal temperature of the first step were calculated and results are shown in Fig. 5b. Reasons that the specific capacitance of the $NiCo_2S_4$/rGO composite electrodes depends on hydrothermal temperature of the first step lie in following facts. The morphology formation process is involved in the following three steps: nucleation, nanosheet formation, and flower-like particle assembly[37,38]. $NiCo_2S_4$ nuclei were first formed through the decomposition of nickel/cobalt complex at elevated temperature. The driving force of the nuclei at low temperature is too weak to form the interconnected $NiCo_2S_4$ nanosheets over rGO, which lead to the lower specific capacitance of the composite at 90°C. When obtaining more energy and driving force with increasing temperature, the nuclei began to grow into nanosheets. Finally, the nanosheets self-assembled into flower-like particle owing to the reduction of surface free energy at

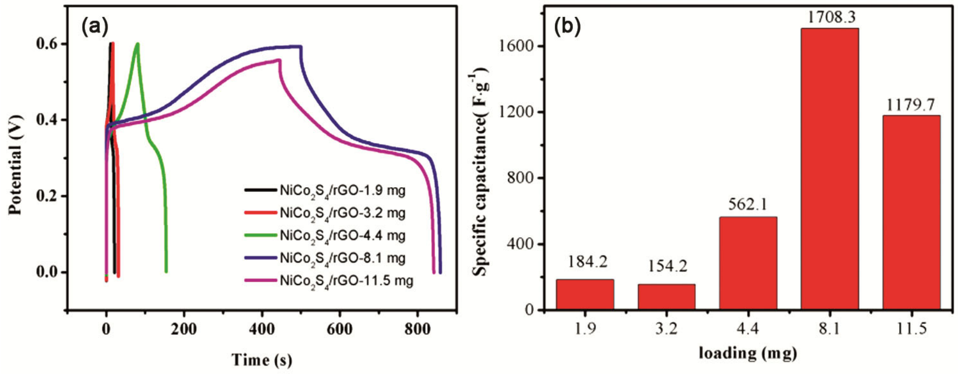

Fig. 4 — (a) GCD curves of the $NiCo_2S_4$/rGO composite electrodes with different mass loadings (10 $mA{\cdot}cm^{-2}$). (b) Histogram of the specific capacitance calculated from the GCD curves.

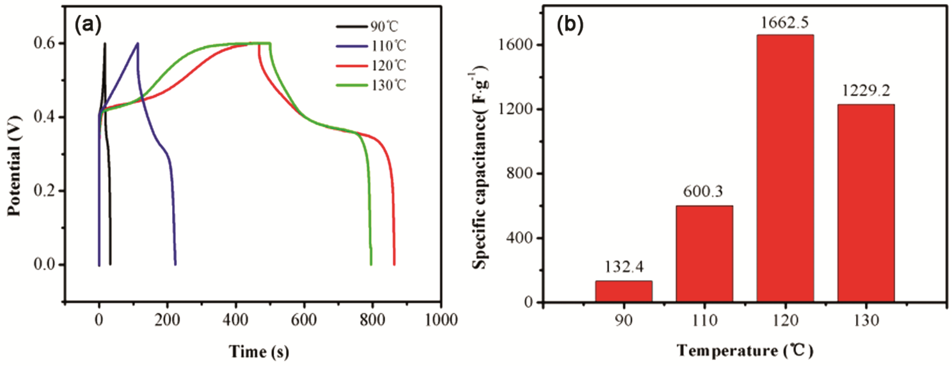

Fig. 5 — (a) The GCD curves of the $NiCo_2S_4$/rGO composite electrodes prepared at different hydrothermal temperature of the first step. (10 $mA{\cdot}cm^{-2}$). (b) Histogram of the specific capacitance of the $NiCo_2S_4$/rGO composites prepared at different hydrothermal temperature.

120°C[38]. When temperature further increased, the nickel/cobalt complex released metal ions slowly and contributed to the growth of nuclei and nanosheets, leading to larger primary particles and thicker petals for the precursors. Therefore, specific surface areas and the active sites on the surface of the $NiCo_2S_4$/rGO composite electrode were significantly reduced, which is responsible for the dramatically decline of the specific capacitance of the composite at 130°C [39].

Electrochemical properties test of the $NiCo_2S_4$ /rGO composite electrode

CV was carried out to study the electrochemical capacitive performances of the as-prepared $NiCo_2S_4$/rGO composite electrode at different scan rates, and results were shown in Fig. 6a. All of the CV curves exhibit very broad redox peaks corresponding to the redox reactions of Co^{3+}/Co^{2+} and Ni^{3+}/ Ni^{2+} couples, which confirms a typical pseudocapacitive behavior of $NiCo_2S_4$. The anodic/cathodic peaks shift towards more positive/negative potential as the scan rate increases from 1 to 35 $mV{\cdot}s^{-1}$. This phenomenon can be attributed to the internal impedance and polarization effect of which the charge transfer rate is faster than the ion diffusion rate at electrode/electrolyte interface[40]. However, the profile of the CV curves at different scan rates can be maintained without obvious deformation, which is indicative of fast interfacial charge transfer and good rate performance, and the composite can achieve charge and discharge at high current density.

Fig. 6b shows the GCD curves of the $NiCo_2S_4$/rGO composite electrode at current densities of 7.5, 10, 15, 20 and 30 $mA{\cdot}cm^{-2}$. The calculated specific capacitance is 2293.4, 1974.7, 1922.5, 1687.2 and 1385.7 $F{\cdot}g^{-1}$, respectively. The reason for the specific capacitance decreases with increasing current densities may be that it is difficult for OH^- ions in the electrolyte to enter the electrode material at high current density, which causes only outside electric-active substances to take part in the redox reaction. All of the GCD curves have obvious platform part at around 0.3 V, which is consistent with the above CV results. The $NiCo_2S_4$/rGO composite electrode remains at 1385.7 $F{\cdot}g^{-1}$ at 30 $mA{\cdot}cm^{-2}$ and holds 61.9% retention of the capacity when the rate increases from 7.5 to 30 $mA{\cdot}cm^{-2}$, implying good rate capability.

Performance test of asymmetric supercapacitor

Fig. 7a exhibits CV curves of AC negative electrode and the $NiCo_2S_4$/rGO composite electrode at a scan rate of 5 $mV{\cdot}s^{-1}$. The CV of the AC electrode shows a nearly rectangular shape without any noticeable redox peaks from –1.0 to 0 V, indicating excellent EDLC behavior for the AC electrode. In the potential range of –0.2 to 0.6 V, the behavior of the $NiCo_2S_4$/rGO composite electrode deviates from the rectangular shape with a pair of redox peak, indicative of the ideal pseudocapacitive behavior for the $NiCo_2S_4$/rGO composite. As the potential windows of the AC and the $NiCo_2S_4$/rGO composite electrodes are –1 to 0 V and −0.2 to 0.6 V, respectively. The total cell voltage can be expressed as the sum of the potential range for AC and the $NiCo_2S_4$/rGO composite, therefore a wide potential window of 1.6 V can be expected.

Fig. 7b shows the GCD curves at current densities from 7.5 to 25 $mA{\cdot}cm^{-2}$ of the $NiCo_2S_4$/rGO //AC asymmetric supercapacitor. The symmetric shape of the GCD with obvious plateau, which is associated with the reversible Faradaic reactions, reflects the combined electrochemical features of the AC and the $NiCo_2S_4$/rGO composite. In addition, the initial voltage

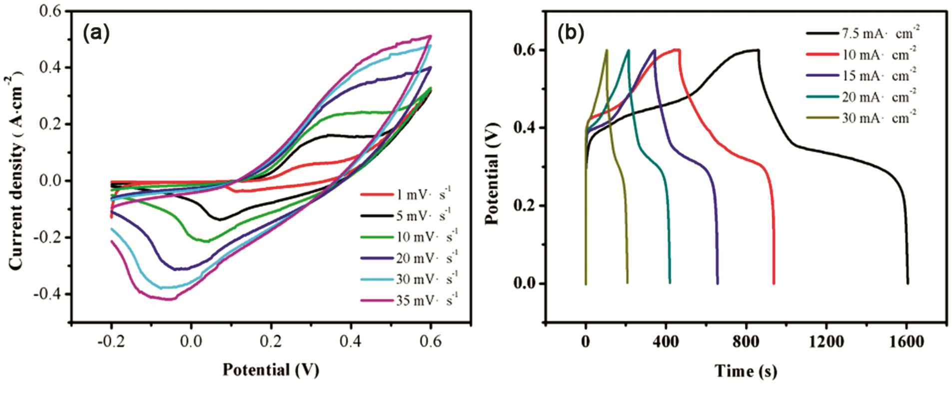

Fig. 6 — (a) CV curves for the $NiCo_2S_4$/rGO composite electrode at different scan rates. (b) GCD curves of the $NiCo_2S_4$/rGO composite electrode at different current densities.

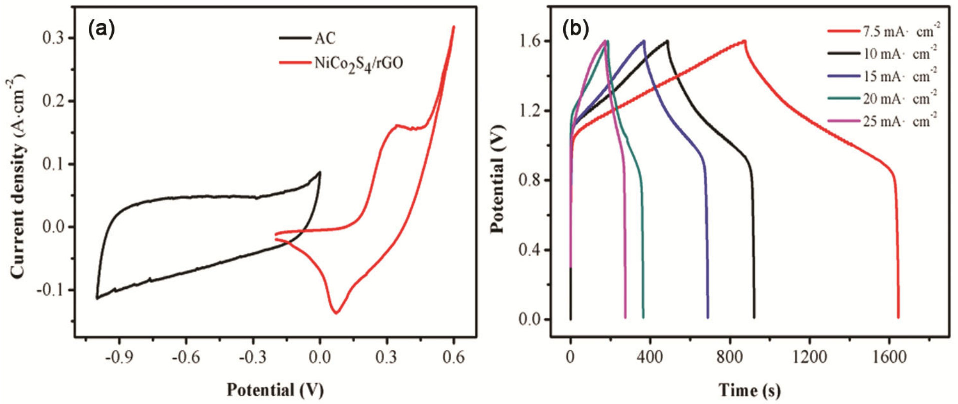

Fig. 7 — (a) CV curves of AC negative electrode and the $NiCo_2S_4$/rGO composite electrode at 5 $mV\cdot s^{-1}$. (b) GCD curves of the $NiCo_2S_4$/rGO //AC asymmetric supercapacitor at different current densities.

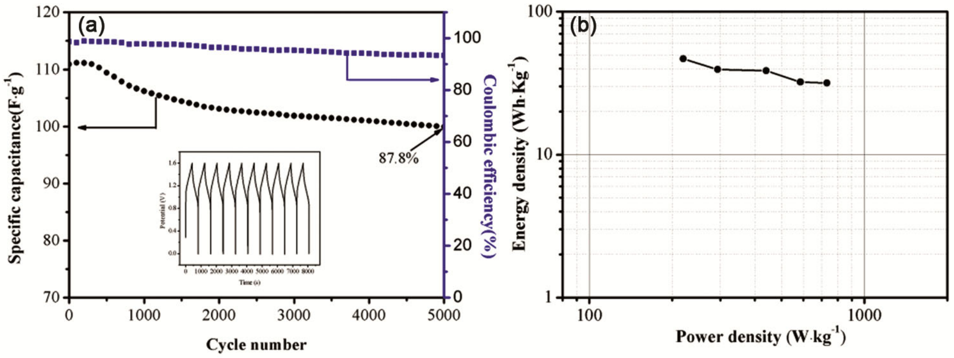

Fig. 8 — (a) Cycling stability curve and coulombic efficiency curve of the $NiCo_2S_4$/rGO //AC asymmetric supercapacitor at a current density of 10 $mA\cdot cm^{-2}$. The inset is the GCD curve of the last 10 cycles. (b) Ragone plot correlating energy density and power density.

loss (*i.e.* IR drop) observed on the discharge curve is rather small, demonstrating low internal resistance and fast I-V response in the supercapacitor[41]. The calculated specific capacitance at current densities of 7.5, 10, 15, 20, and 25 $mA\cdot cm^{-2}$ is 131.5, 111.2, 108.9, 90.6 and 89.3 $F\cdot g^{-1}$, respectively. The $NiCo_2S_4$/ rGO //AC asymmetric supercapacitor displays good rate performance, it can still maintain 66.1% capacitance of the current density of 7.5 $mA\cdot cm^{-2}$ at 25 $mA\cdot cm^{-2}$. The decreasing specific capacitance with the augment of current density is associated with the insufficient time to take part in the redox reactions for electrolyte ions [40].

Fig. 8a shows the cycling stability of the $NiCo_2S_4$/rGO //AC asymmetric supercapacitor, and the inset is the GCD curves of the last 10 cycles. The capacitance of the supercapacitor shows increases in the initial cycles, and then a slight decrease and remains quite constant with cycle number, indicating excellent cycling stability of the $NiCo_2S_4$/rGO //AC asymmetric supercapacitor. The initial increase of the capacitance is due to the electrode activation process. The decrease of the capacitance for the following cycles is probably due to the dissolution and detachment of the active material into the electrolyte during the long-time cycling [41]. After 5000 cycles, the specific capacitance of the $NiCo_2S_4$/rGO //AC device can still maintain 87.8% of the initial value at a current density of 10 $mA\cdot cm^{-2}$, indicating the good cycling stability, and the coulomb efficiency is maintained at 93.4%.

Fig. 8b shows the Ragone plot of the $NiCo_2S_4$/rGO //AC asymmetric supercapacitor based on GCD tests in a voltage window of 0-1.6 V. It is worth noting that the maximum energy density obtained for our asymmetric supercapacitor is 46.8 $Wh\cdot kg^{-1}$ at a power density of 219.5 $W\cdot kg^{-1}$, and the maximum power density obtained for our asymmetric supercapacitor is 731.6 W kg^{-1} at an energy density of 31.8 Wh kg^{-1}.

Conclusion

A two-step hydrothermal method of growing flower-like $NiCo_2S_4$ /rGO composite on the Ni foam with hierarchical structures was demonstrated in this work. rGO increases the interconnected surface area of electrode material, which contributes to reduce the ion diffusion and charge transfer resistance. The

$NiCo_2S_4$/rGO composite electrode prepared by adjusting the hydrothermal conditions displays a high specific capacitance of 1974.7 $F{\cdot}g^{-1}$ at the current density of 10 $mA{\cdot}cm^{-2}$. The assembled $NiCo_2S_4$/rGO //AC asymmetric supercapacitor exhibits superior cycling stability (capacitance retention of 87.8% after 5000 cycles) at a current density of 10 $mA{\cdot}cm^{-2}$ and achieves an improved energy density of 31.8$Wh{\cdot}kg^{-1}$ at a power density of 731.6$W{\cdot}kg^{-1}$, indicating the great potential of becoming electrode materials for energy storage devices.

Acknowledgment

This work was supported by Henan Provincial Key Research Projects for Colleges and Universities (No. 24B150046).

References

1 Chodankar N R, Gund G S, Dubal D P & Lokhande C D, *RSC Adv*, 4 (2014) 61503.
2 Kamble G P, Rasal A S, Gaikwad S B, Gurav V S, Chang J Y, Kolekar S S, Ling Y C & Ghule A V, *ACS Appl Nano Mater, 4* (**2021**) 12702 .
3 Jiang H, Lee P S & Li C, *Energy Env Sci*, 6 (2013) 41.
4 Banda H, Aradilla D, Benayad A, Chenavier Y, Daffos B, Dubois L & Duclairoir F, *J Power Sources*, 360 (2017) 538.
5 Mirzaee M & Dehghanian C, *Mat Today Energy*, 10 (2018) 68.
6 Zhang M, Zheng H, Zhu H, Zhang M, Liu R, Zhu X, Li X & Cui H, *J Alloy Compd*, 901 (2022) 163633.
7 Yuan L, Wan C, Ye X & Wu F, *Electrochim Acta*, 213 (2016) 115.
8 Yu G, Hu L, Liu N, Wang H, Vosgueritchian M, Yang Y, Cui Y & Bao Z, *Nano Lett*, 11 (2011) 4438.
9 Zhang X, Ma L, Gan M, Fu G, Jin M, Lei Y, Yang P & Yan M, *J Power Sources*, 340 (2017) 22.
10 Liu J, Jiang J, Cheng C, Li H, Zhang J, Gong H & Fan H, *Adv Mat*, 23 (2011) 2076.
11 Kumar L, Chauhan H, Yadav N, Yadav N, Hashmi S & Deka S, *ACS Appl Energy Mat, 1* (**2018)** 6999.
12 Sahoo K, Acharyya P, Singh N K, Pal A, Negishi Y & Pal T, *ACS Omega,* 2 (2017) 6576.
13 Hao J, Liu H, Han S & Lian J, *ACS Appl Nano Mater, 4* (2021) 1330.
14 Ren B, Zhang X, An H, Ding S, Zhang H, Zeng X, Wang X, Fan M & Yang X, *J Energy Storage*, 59 (2023) 106553.
15 Wu W, Zhao C, Wang C & Zhu J, *Appl Surf Sci*, 563 (2021) 150324.
16 Song Y, Wu H, Sun B, Liu M, Ren W, Xu Y, Cao Y & Chen C, *J Energy Storage*, 72 (2023) 108442 .
17 Hu W, Chen R, Xie W, Zou L, Qin N & Bao D, *ACS Appl. Mater. Interfaces*, 6 (2014) 19318.
18 Sonia Y K, Srivastav S & Meher S K , *Langmuir*, 39 (2023) 9111.
19 Panicker N J & Sahu P P, *Diam Relat Mater*, 136 (2023) 109936.
20 Ye Y, Luo Y, Lou J, Chen X, Cheng Y, Xia J, Li Y & Guo K, *ACS Appl Energy Mater, 6* (2023) 6742.
21 Abdel-Salam A I, Attia S Y, El-Hosiny F I, Sadek M A, Mohamed S G & Rashad M M, *Mat Chem Phy*, 277 (2022) 125554.
22 Hoa N V, Dat P A, Chi N V & Quan L H, *J Sci Adv Mat Dev*, 6 (2021) 569.
23 Li Z, Ji X, Han J & Guo R, *J Colloid Interface Sci*, 477 (2016) 46.
24 Liu P, Sui Y, Wei F, Qi J, Meng Q, Ren Y & He Y, *J Mat Sci Mat Ele*, 30 (2019) 19077.
25 Gong X, Cheng J, Ma K, Liu F, Zhang L & Zhang X, *Mat Chem Phys*, 173 (2016) 317.
26 Chen X, Chen D, Guo X, Wang R & Zhang H, *ACS Appl Mat Interface*, 9 (2017) 18774.
27 Meng X, Wu Z, Chen L, Li J, Jing Y & Huo S, *J Phy Chem Solid*, 178 (2023) 111375.
28 Zhang Y, Ma M, Yang J, Sun C, Su H, Huang W & Dong X, *Nanoscale*, 6 (2014) 9824.
29 Panicker N J, Dutta J C & Sahu P P, *Chem Eng J*, 463 (2023) 142376.
30 Dong M, Wang Z, Yan G, Wang J, Guo H & Li X, *J Alloy Comp*, 822 (2022) 153645.
31 Peng W, Chen H, Wang W, Huang Y & Han G, *Curr Appl Phy*, 20 (2020) 304.
32 Huang X & Gou L, *Appl Surf Sci*, 487 (2019) 68.
33 Qu G, Wang Z, Zhang X, Zhao S, Wang C, Zhao G, Hou P & Xu X, *Chem Eng J*, 429 (2022) 132406.
34 Jing C, Guo X, Xia L, Chen Y, Wang X, Liu X, Dong B, Dong F, Li S & Zhang Y, *Chem Eng*, 379 (2020) 122305.
35 Wu Z, Wang D, Ren W, Zhao J, Zhou G, Li F & Cheng H, *Adv Fun Mat*, 20 (2010) 3595.
36 Yuan J & Zeng W, *Mat Lett*, 330 (2023) 133338.
37 Zhao F, Xie D, Song X, Wu H, Zhang Q, Zou J & Zeng X, *Appl Surface Sci*, 539 (2021) 148260.
38 Su Z, Zhang X, Shi D & Zhang X, *J Mat Sci Mat Ele*, 34 (2023) 628.
39 Cao Z, Liu C, Huang Y, Gao Y, Wang Y, Li Z, Yan Y & Zhang M, *J Power Sources*, 449 (2020) 227571.
40 Huang D, Lu Z, Liu X, Gao J, Chen Z, Wang X & Fu X, *Appl Surface Sci*, 605 (2022) 154707.
41 Zhao C, Ren F, Xue X, Zheng W, Wang X & Chang L, *J Elec Chem*, 782 (2016) 98.